ACS APPLIED MATERIALS & INTERFACES

Research Article

www.acsami.org

Nitrogen-Enriched Porous Carbon Coating for Manganese Oxide Nanostructures toward High-Performance Lithium-Ion Batteries

Jiangan Wang,*[,†] Cunbao Zhang,[†] and Feiyu Kang[‡]

[†]State Key Laboratory of Solidification Processing, Center for Nano Energy Materials, School of Materials Science and Engineering, Northwestern Polytechnical University, Xi'an 710072, China

[‡]Institute of Advanced Materials Research, Graduate School at Shenzhen, Tsinghua University, Shenzhen 518055, China

Supporting Information

ABSTRACT: Manganese oxides are promising high-capacity anode materials for lithium-ion batteries (LIBs) yet suffer from short cycle life and poor rate capability. Herein, we demonstrate a facile in situ interfacial synthesis of core−shell heterostructures comprising nitrogen-enriched porous carbon (pN-C) nanocoating and manganese oxide (MnO_x) nanotubes. When MnO_x/pN-C serves as an anode material for LIBs, the pN-C coating plays multiple roles in substantially improving the lithium storage performance. In combination with the nanosized structure and nanotubular architecture, the MnO_x/pN-C nanocomposites exhibit an impressive reversible capacity of 1068 mAh g^{-1} at 100 mA g^{-1}, a high-rate delivery of 361 mAh g^{-1} at 8 A g^{-1}, and a stable cycling retention up to 300 cycles. The surface pN-C coating strategy can be extended to design and fabricate various metal oxide nanostructures for high-performance LIBs.

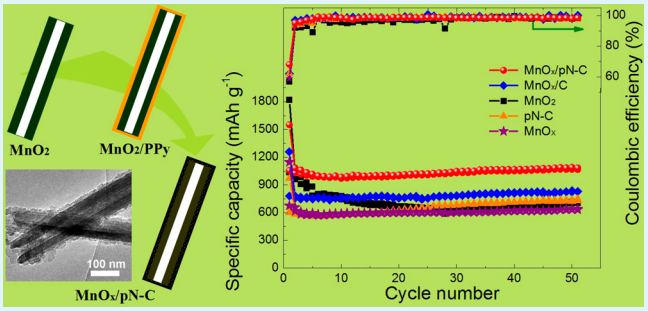

KEYWORDS: *nitrogen-doped carbon, manganese oxide, nanotube, anode, lithium-ion battery*

1. INTRODUCTION

Increasing social concern about fossil depletion and global climate change has stimulated worldwide research interests in the sustainable and renewable energy storage systems.[1] Until now, rechargeable lithium ion batteries (LIBs) remain dominant as power sources in areas from portable electric devices to thriving electric vehicles to smart utility grids due to their high energy density, high voltage, and no memory effect.[2,3] However, the commercial graphite anode suffers from low theoretical capacity (372 mAh g^{-1}) and slow reaction kinetics, which cannot meet the ever-increasing energy demands. Hence, it is imperative to develop advanced anode materials with high reversible capacity, long cycle life, good rate capability, low cost, and environmental benignity. To date, significant achievements have been gained in various promising anode materials with high theoretical capacity, such as metal oxides Sn and Si.[4,5] Among the metal oxides investigated for LIBs, manganese oxides (MnO_x) are received tremendous interest owing to their high theoretical capacity (e.g., 1232 mAh g^{-1} for MnO_2), low discharge plateau (0.3−0.6 V), narrow potential hysteresis, low cost, natural abundance of Mn sources, and eco-friendliness.[5,6] Nevertheless, the critical problems of poor cycling stability and inferior rate capability become major obstacles for practical implementation of MnO_x to LIBs. The reasons for poor cycle life are the substantial volume changes and particle agglomeration during the repetitive lithiation/delithiation processes, resulting in both mechanical failure and loss of electrical connection from the current collector (i.e., pulverization). The other drawback of inferior rate capability of MnO_x results from its extremely low electrical conductivity.

Generally, the most effective strategy to address the above issues of MnO_x requires a combination of carbon hybridization, nanostructuring, and configuration design. This is because carbon hybridization can cushion the large stress caused by volume expansion/contraction, protect the MnO_x from chemical corrosion and agglomeration, and increase the electrical conductivity of the composite.[7,8] Meanwhile, reducing the MnO_x size to nanoscale can accommodate partial volume change, shorten the electron/ion transport distance, and create more contact interfaces that favor the reversible redox reaction between Li^+ and MnO_x.[9,10] Additionally, the structure configuration can influence the electrochemical utilization of active materials at different rate conditions; for example, a stiff carbon framework is not good for Li^+ transport into the interior MnO_x, while MnO_x grown on the exterior surface of carbon matrix may lead to a rapid degradation.[11] Recently, there have been many reports with regard to various MnO_x/C nanocomposites with improved performance, such as MnO_x (e.g., MnO, Mn_3O_4)/C nanorods/nanotubes/nanoplates/nanoparticles,[12−18] MnO_x (e.g., MnO, Mn_3O_4, or MnO_2)/graphene,[8,19−22] MnO_x/carbon nanotubes (CNTs),[11,23−25] and MnO_x/carbon nanofibers.[6,26,27] Table S1 (Supporting Informa-

Received: February 16, 2015
Accepted: April 14, 2015
Published: April 14, 2015

DOI: 10.1021/acsami.5b01388
ACS Appl. Mater. Interfaces 2015, 7, 9185−9194

tion) summarizes the electrochemical performance of MnO_x-carbon composite electrodes. As shown in the table, compared to the graphene, CNTs, carbon nanofibers, and ordered mesoporous carbon that load MnO_x nanoparticles, surface carbon coating is more favorable for MnO_x with large dimensional sizes, such as nanorods and nanotubes. On another hand, the scale-up production may prefer to the low-cost surface carbon coating method. The coating strategy usually includes chemical vapor deposition, hydrothermal method, and some other solution-based chemical precipitation. However, scarcely can the MnO_x/C nanocomposites prepared by these methods surpass a high reversible capacity of 1000 mAh g^{-1} over a 100-cycle test, which is not enough for practical implementation. This may be because most carbon coatings often act as an elastic protecting and electrical conducting layer but scarcely make an electro-active contribution to the overall capacity.

Nitrogen-enriched porous carbon (pN-C) nanostructures, such as pN-C nanofibers,[28,29] N-doped graphene[30] and N-doped CNTs,[31] have been demonstrated to show much improved capacity (e.g., 1363 mAh g^{-1} for pN-C nanofibers[28])) compared to the pristine carbon nanostructures. The heteroatom of nitrogen in the carbon structure can not only enhance the electrochemical activities of carbon but also increase the electrical conductivity for better reaction kinetics. In addition, the porous nanostructures can provide numerous electro-active sites for Li^+ storage. Hence, it would be of particular fascination to combine pN-C with MnO_x nanostructure by constructing a unique heretostructure, aiming to make a full utilization of both components. Some works report the exploitation of MnO_x/nitrogen-doped carbon composites with improved performance; however, in their strategies, carbon structures are used as sacrificial supports for depositing MnO_x nanoparticles.[19,33,34] That is, MnO_x nanoparticles are easy to stay at the exterior surfaces of carbon matrix, which may deteriorate the cycling stability. Alternatively, it is expected that surface pN-C coating strategy can address this critical issue. Nevertheless, it remains a great challenge to develop a general, flexible and effective method to integrate a uniform pN-C coating with different MnO_x structures.

In this work, we report a general solution-based approach to synthesize MnO_x/pN-C core−shell nanostructures. One-dimensional (1D) MnO_2 nanotubes is used to demonstrate this design strategy. Figure 1a illustrates the typical synthesis protocol. The core issue is to chemically form uniform polypyrrole (PPy) coating on the surface of MnO_2 structures via in situ interfacial polymerization using MnO_2 as reactive templates. MnO_x/pN-C nanocomposite with well-constructed core−shell nanotubular configuration can be obtained after a simple thermal pyrolysis (carbonization). Benefiting from the multiple functions of the pN-C nanoshells and the unique nanoarchitecture (Figure 1b), the MnO_x/pN-C nanocomposite exhibits superior lithium-storage performance, such as high reversible capacity of ∼1100 mAh g^{-1} at 100 mA g^{-1}, excellent rate capability and long-span cyclability

2. EXPERIMENTAL SECTION

2.1. Material Synthesis. All chemical reagents were of analytical grade and used as received. MnO_2 nanotubes were prepared based on our previous work,[35] via a hydrothermal reaction in a $KMnO_4$ + HCl aqueous system at 150 °C for 12 h. The synthesis of MnO_2/PPy was carried out through an in situ chemical reaction between MnO_2 and pyrrole monomers in an acidic solution. Typically, 100 mg of the as-collected brown MnO_2 powder was dispersed in 20 mL of 0.1 M HCl solution under ultrasonication for 30 min. Afterward, 25 μl of pyrrole monomers was added dropwise to the above suspension under rigorous magnetic stirring. The color of the suspension evolved quickly from brown to black. The in situ reaction was maintained for 4 h to complete the polymerization process. The resulting black products were filtered and washed using ethanol and deionized water three times, respectively. Then the as-received MnO_2/PPy composites were heated to 600 °C at a ramping rate of 3 °C/min under the protect of N_2 gas flow, and hold at this temperature for 2 h. To clarify the role of pN-C coating in the electrochemical performance, we fabricated MnO_x/C nanostructures by using glucose as carbon precursor with other conditions unchanged according to ref 15. Meanwhile, pure PPy nanotubes were synthesized by controlling the MnO_2/pyrrole molar ratio at 1:1,[36] and the MnO_x and pN-C were prepared from the MnO_2 and PPy under the same carbonization treatment.

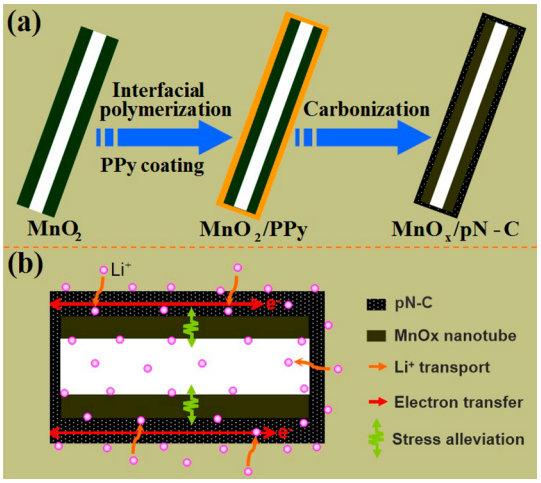

Figure 1. Schematic presentation of the (a) synthesis and (b) energy storage characteristics of MnO_x/pN-C nanotubular heretostructure.

2.2. Materials Characterization. X-ray powder diffraction (XRD, Rigaku D/Max 2500PC, Japan) was performed to confirm the crystallographic information on the samples. Raman spectrum was recorded on Renishaw Invia RM200 (England) at room temperature in the spectral range of 200−2500 cm^{-1}. The mass content of the carbon coating was determined using thermogravimetric analysis (TGA, TA Instruments SDT-Q600). The morphology and structure of the samples were observed on a field emission scanning electron microscopy (FE-SEM, LEO-1530) and a high-resolution transmission electron microscopy (HRTEM, JEOL 2010). The pore structures were characterized by N_2 adsorption measurement at 77 K (Belsorp, Japan). Brunauer−Emmett−Teller (BET) method and nonlocal density functional theory (NLDFT) calculation were used to determine the specific surface area and the corresponding pore size distribution. The surface chemistry of the nanocomposites was investigated using a PHI Quantera Imaging X-ray photoelectron spectroscopy (XPS).

2.3. Electrochemical Evaluation. The electrochemical properties were measured using coin-type (CR2032) half cells. The working electrodes were fabricated by mixing 75 wt % of active materials with 15 wt % of carbon black and 10 wt % of poly(vinylidene fluoride) (PVDF) binder in *N*-methyl-2-pyrrolidone (NMP) solvent. The resultant slurry was uniformly painted onto a copper foil by a doctor blade. The obtained electrode was dried overnight at 100 °C in a vacuum oven. Coil cells were assembled in an argon-filled glovebox with a metal Li plate as the counter electrode, Celgard 2320 as the separator, and a solution of 1.0 $LiPF_6$ in ethylene carbonate (EC)/diemethyl carbonate (DMC)/diethyl carbonate (DEC) (1:1:1 by volume) as the electrolyte. Cyclic voltammetry (CV) measurement was performed on a Princeton electrochemical workstation. Galvanostatic charge/discharge tests were carried out on a Land Battery Testing system at various current densities between cutoff potentials of 0.01 and 2.50 V vs Li/Li^+.

DOI: 10.1021/acsami.5b01388
ACS Appl. Mater. Interfaces 2015, 7, 9185−9194

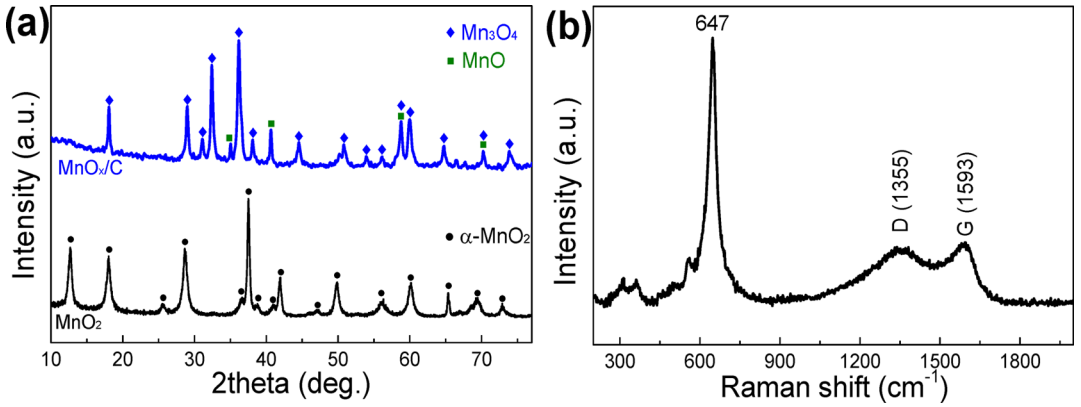

Figure 2. (a) XRD patterns of MnO_x/pN-C and MnO_2. (b) Raman spectrum of MnO_x/pN-C.

3. RESULTS AND DISCUSSION

PPy is an excellent carbon precursor candidate that contains a high theoretical content of nitrogen (~21 wt %).[28] The major challenge in this work is to uniformly deposit PPy on MnO_2 surfaces. There are a few reports trying to coat PPy on MnO_x nanorods using $FeCl_3$[37] or $Na_2S_2O_8$[18] as oxidants under the assistance of surfactants. Because the polymerization occurs throughout the bulk solution, these methods would give rise to nonuniform PPy coating onto nanorods and undesirable PPy nanoparticles without connection to the nanorods. In addition, the use of organic surfactants in their studies may be detrimental to the environment. In our previous study,[36] MnO_2 was found to have the capability to polymerize pyrrole monomers in an acidic condition, because the chemical oxidative potential of MnO_2 (i.e., $MnO_2 + 4H^+ + 2e \rightarrow Mn^{2+} + 2H_2O$, $\varphi = 1.23$ V) is much higher than that of pyrrole momomers (0.7 V). In other words, PPy can be chemically formed based on in situ interfacial reaction using MnO_2 structures as the oxidative templates. This characteristic offers a general strategy to uniformly deposit PPy coating on a vast variety of MnO_2 structures regardless of their morphologies. The thickness of the PPy coating can be well-controlled by adjusting the reactant ratio of MnO_2/pyrrole. Using this design strategy, as illustrated in Figure 1a, we manage to chemically coat uniform PPy layer on the chosen MnO_2 nanotubes, and the final MnO_x/pN-C product is obtained by a simple subsequent carbonization.

Figure 2a shows the XRD patterns of MnO_x/pN-C nanocomposite and the pristine MnO_2. All the peaks of the pristine MnO_2 can be readily indexed to the pure tetragonal phase of α-MnO_2 (JCPDS 44-0141).[35] After a carbonization process, the main diffraction peaks are well-assigned to the hausmannite Mn_3O_4 phase with tetragonal structure (JCPDS 89-4837).[7] In addition, there are some minor peaks that can be ascribed to the cubic phase of MnO (JCPDS 07-0230).[20,38,39] The result reveals that α-MnO_2 phase has undergone reduction transitions in the inert atmosphere accompanying with oxygen release from MnO_2.[15] No diffraction peak of carbon is observed in the pattern, which may be ascribed to the low content and amorphous state of carbon. The presence of carbon can be detected easily using Raman test because carbon is of highly Raman-active nature. As shown in Figure 2b, the broad peaks displayed at 1355 and 1593 cm^{-1} are assigned to the D and G bands of pN-C, respectively. The high intensity of the D band confirms the amorphous (disordered) structure of carbon, demonstrating that many defects are abundant in the pN-C. The fundamental Raman scattering peak of MnO_x at 647 cm^{-1} is characteristic of the Mn−O vibration mode.[8,19,40] The Raman result validates the presence of carbon and MnO_x components in the nanocomposite, and the carbon content is estimated to be approximately 18.6 wt % according to the TGA result (Figure S1, Supporting Information).

The microstructure of the pristine MnO_2 and MnO_x/pN-C was characterized by SEM and TEM. The panoramic morphology of the pristine MnO_2, as shown in Figure 3a, is,

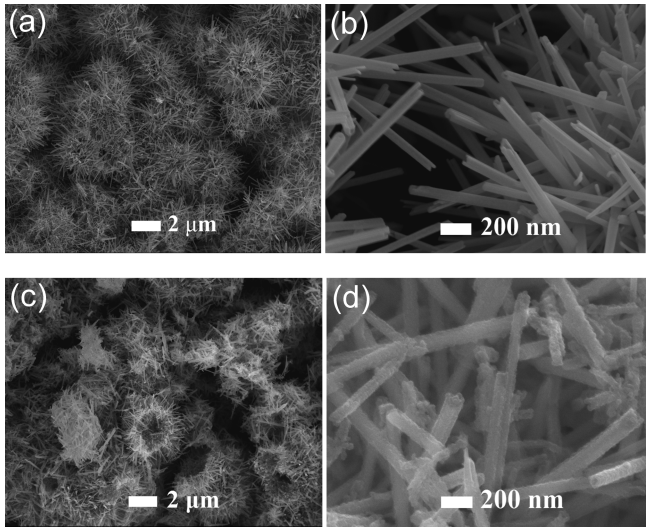

Figure 3. SEM images of (a and b) MnO_2 and (c and d) MnO_x/pN-C nanocomposite.

on a large scale, composed of hollow urchin-shape microspheres with diameters in 5−10 μm. From the high-magnification SEM image of Figure 3b, the three-dimensional (3D) microspheres are observed to be assembled by 1D radial nanotubes with smooth surface and clear open ends. During the preparation process of the MnO_x/pN-C nanocomposite, the microspheres are broken into pieces with hollow cavities being visible (Figure 3c). This is due to the 3D assembly of microspheres is driven by weak chemical interactions of van der Waals forces and hydrogen bonds between nanotubes,[35] which are easily ruptured by physical sonication. Nevertheless, the building blocks of 1D nanotubes are well-preserved (Figure 3d), the surfaces of which become somewhat rough after pN-C coating. More structural details about the MnO_x/pN-C nanocomposite are obtained from TEM imaging. As shown

DOI: 10.1021/acsami.5b01388
ACS Appl. Mater. Interfaces 2015, 7, 9185−9194

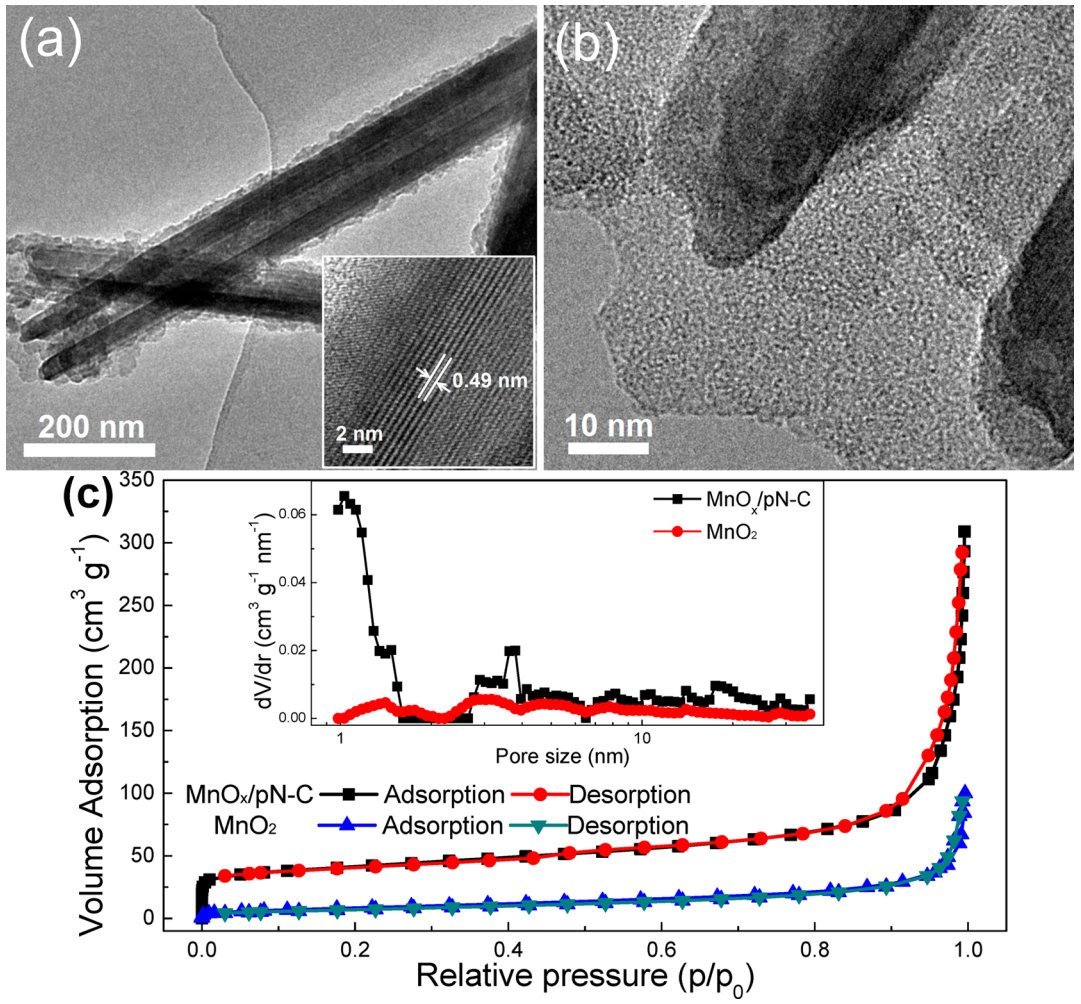

Figure 4. (a and b) TEM images of MnO_x/pN-C nanocomposite and (a, inset) the corresponding HRTEM. (c) N_2 adsorption/desorption isotherms and (inset) pore size distribution of MnO_2 and MnO_x/pN-C composite.

in Figure 4a, the MnO_x/pN-C clearly exhibits a typical nanotubular structure. The average diameter and the wall thickness of the nanotubes are ca. 120 and 40 nm, respectively. Moreover, a very uniform pN-C shell with a thickness of 10−15 nm is coated on the exterior surface of the MnO_x nanotubes, constructing unique core−shell configuration. The HRTEM image of the MnO_x (inset) exhibits well-resolved lattice fringes with a typical interplane distance of 0.49 nm belonging to the (101) planes of Mn_3O_4. The HRTEM of the carbon shell (Figure 4b) exhibits a porous structure having a large quantity of nanopores inside. The formation of the porous structure can be ascribed to the pyrolysis of PPy and possibly the release of gases during the reduction of MnO_2. The porous characteristics were investigated by N_2 adsorption/desorption measurement. Figure 4c shows the resulting isotherms of MnO_2 and MnO_x/pN-C nanocomposite. The BET specific surface area and pore volume of the nanocomposite are 148 $m^2\ g^{-1}$ and 0.478 $cm^3\ g^{-1}$, respectively, which are much larger than those of MnO_2 (33 $m^2\ g^{-1}$ and 0.155 $cm^3\ g^{-1}$). From the corresponding pore-size distribution in the inset of Figure 4c, the MnO_x/pN-C nanocomposite possesses much larger amount of both micropores and mesopores than MnO_2. Based on the TGA result, the specific surface area of pN-C can be estimated to be about 651 $m^2\ g^{-1}$. The highly porous structure of the MnO_x/pN-C nanocomposite is beneficial in providing more electro-active sites for Li^+ storage, and facilitating easy access of electrolyte ions to the active materials with small diffusion resistance.

XPS was used to examine the surface elemental composition and chemical state of the MnO_x/pN-C nanocomposite. The survey spectrum in Figure 5a shows the presence of C, N, Mn, and O element signals with no trace of impurities. The core level spectrum of Mn 2p (Figure 5b) displays a Mn $2p_{3/2}$ peak at 641.7 eV and a Mn $2p_{1/2}$ peak at 653.4 eV with a spin-energy separation of 11.7 eV, which agrees well with those reported for MnO_x.[23,34,41] The core level spectrum of N 1s in Figure 5c can be readily resolved into two subpeaks centered at 398.4 and 400.2 eV, representing hexagonal pyridinic nitrogen (N-6) and pentagonal pyrrolic nitrogen (N-5), respectively.[28,32,42,43] The C−N bonding structures are also confirmed by the C 1s core level spectrum analysis. As shown in Figure 5d, the spectrum can be deconvolved into four components centered at 284.6, 285.5, 286.6, and 288.8 eV, corresponding to sp^2−sp^2C, N−sp^2C, N−sp^3C, and C−O type bonds, respectively.[18,19] This indicates that a large portion of N atoms in the PPy ring were converted into pyridinic nitrogen during carbonization process. These distinctive N-configurations are most likely to distribute at the basal-planes and edges in the graphene structure, as illustrated in inset of Figure 5c, thereby creating a large amount of edge/basal defects that hold higher electronegativity and

DOI: 10.1021/acsami.5b01388
ACS Appl. Mater. Interfaces 2015, 7, 9185−9194

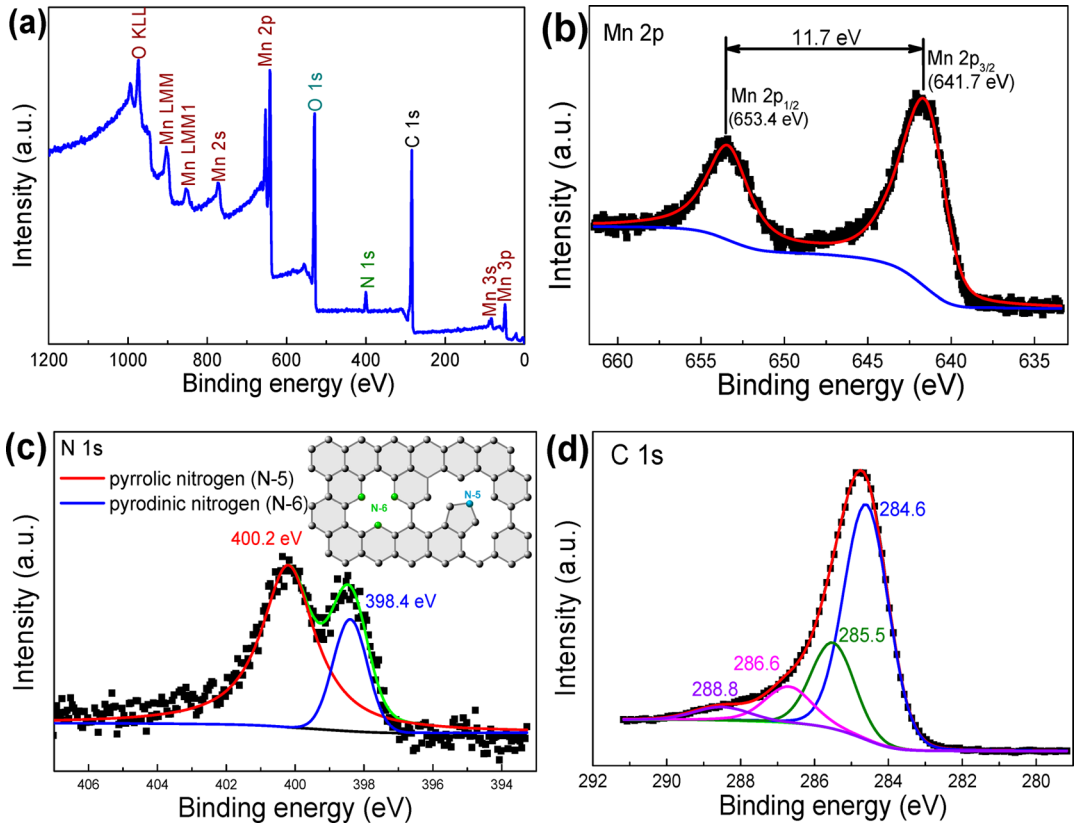

Figure 5. (a) The survey spectrum of the MnO_x/pN-C nanocomposite and the core level spectra of (b) Mn 2p, (c) N 1s, and (d) C 1s.

higher reactivities for Li^+ penetration/adsorption.[30,32] In addition, the N-6 configuration is sp^2-hybridized, which can enhance the electron donor/acceptor properties (i.e., conductivity) of neighboring carbon atoms.[29] More importantly, the high nitrogen content of the PPy precursor can ensure a high level of nitrogen doping in the pN-C layer, the N/C atomic ratio of which is measured to be 11.4% from the XPS results. The high-level content of nitrogen in the pN-C is supposed to be favorable for enhanced electrochemical properties, such as Li^+ storage capacity and rate capability.

The electrochemical performance of MnO_x/pN-C nanocomposites is evaluated as anode materials for Li-ion batteries. CV measurement was first carried out to understand the electrochemical behavior during the charge/discharge cycling. Figure 6a,b exhibit the first three CV curves of the MnO_x/pN-C nanocomposite and pure MnO_2 nanotube electrodes at a scan rate of 0.2 mV s^{-1} in the range of 0.0−2.5 V, respectively. As shown in Figure 6a, the cathodic peak at around 0.65 V in the first cycle is associated with the irreversible decomposition of electrolyte accompanying with the formation of the solid electrolyte interface (SEI) layer on the electrode surface.[7,34,38,44] The reduction process below 0.4 V with a sharp peak at 0.16 V corresponds to a multistep electrochemical lithiation reaction of MnO_x with Li. It is worthy to point out that the formation of SEI layer in the nanocomposite electrode is prior to the reduction of MnO_x. As for the pure MnO_2 electrode (Figure 6b), a broad cathodic peak centered at 0.15 V is ascribed to the concurrent process of the formation of SEI layer and the reduction of MnO_2. The big difference indicates that the wrapped pN-C coating can modify the surface chemistry of MnO_x, which may be favorable for building stable electrode/electrolyte interfaces. The preformation of the SEI layer can also safeguard the structural integrity of the nanocomposite during the cycling operation. From the second and onward cycles, the main reduction peak shifts to 0.43 and 0.38 V for the MnO_x/pN-C nanocomposite and pure MnO_2 electrodes, respectively. It can be observed that the peak of the second cycle is nearly overlapped to that of the third cycle for the nanocomposite electrode. However, there is a significant decrease in the peak intensity for the pure MnO_2 electrode in the third cycle. This evidence suggests that the nanocomposite electrode shows better cycling stability and reversibility than the MnO_2 electrode. During the anodic scan, the main peak at around 1.30 V is ascribed to the oxidation (delithiaton) reaction of metallic Mn. The charge potential is much lower than those of other metal oxides, such as Fe_3O_4 (1.7 V), Fe_2O_3 (1.6 V), Co_3O_4 (2.0 V), CoO (1.8 V), NiO (1.9 V), CuO (2.1 V), and RuO_2 (2.4 V).[5,15] The low potential would lead to a higher working voltage when the anode serves in a full cell, which can therefore offer a higher energy density. In addition, a small oxidation peak at around 2.1 V is observed in the MnO_x/pN-C anode, indicating the Mn^{2+} in the nanocomposite can be reoxidized to a higher oxidation state. The unique phenomenon can be attributed to the conductive pN-C layers, which enhance the charge-transfer kinetics and the reaction activity that can generate more capacity.[18,20] According to the above description, the formation of Mn and Li_2O and the regeneration of MnO_x can be expressed by the following conversion reaction:

$$MnO_x + 2xLi \leftrightarrow xLi_2O + Mn$$

As an effort to elucidate the improved lithium storage performance of the MnO_x/pN-C electrode, we performed galvanostatic charge/discharge cycling tests. Figure 6c and Figure S2 (Supporting Information) shows the typical charge/

DOI: 10.1021/acsami.5b01388
ACS Appl. Mater. Interfaces 2015, 7, 9185−9194

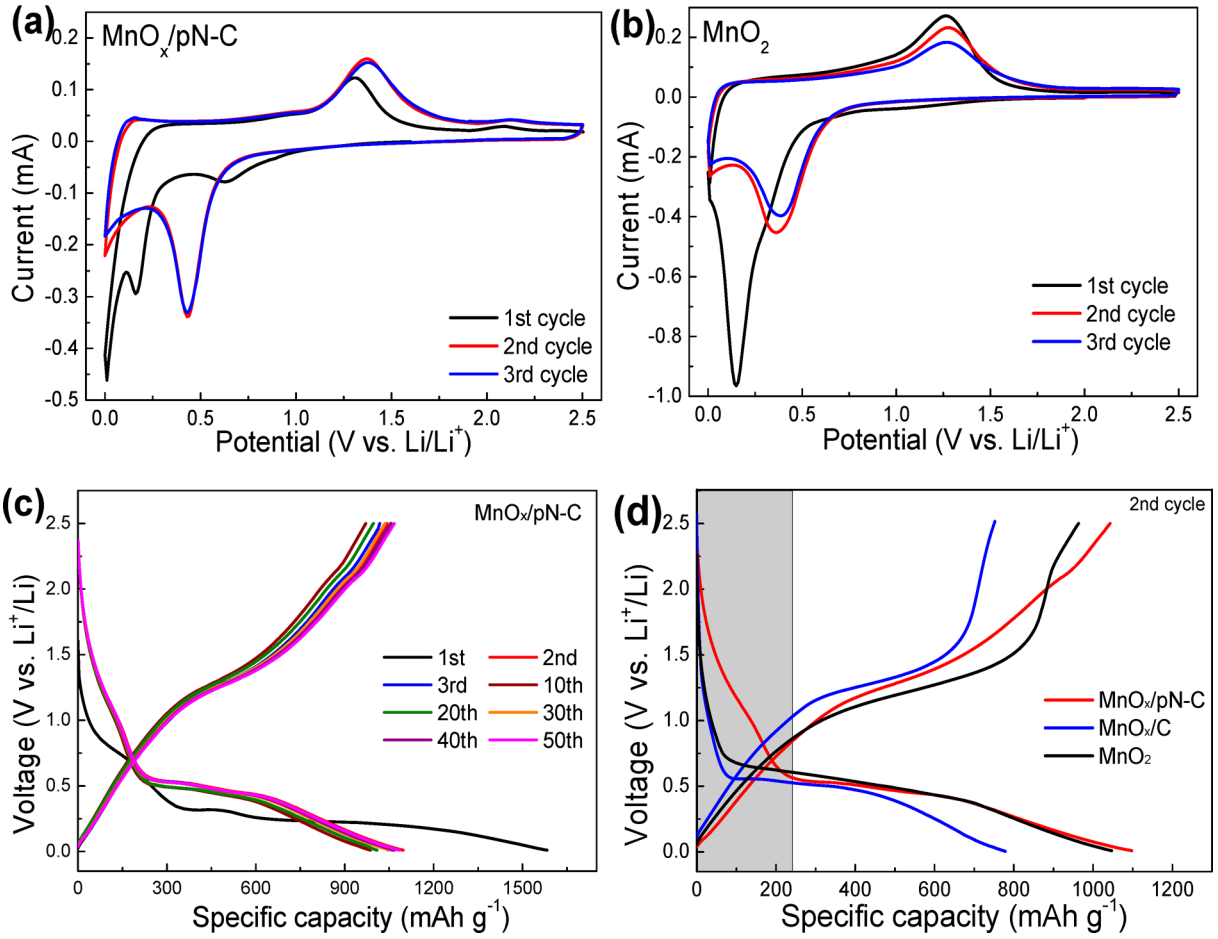

Figure 6. CV curves of (a) MnO_x/pN-C nanocomposite and (b) pure MnO_2 nanotube electrodes at a scan rate of 0.2 mV s^{-1}. (c) Galvanostatic charge/discharge curves of MnO_x/pN-C nanocomposite electrode at a current density of 100 mA g^{-1}. (d) A comparison of the voltage profiles of the MnO_x/pN-C, MnO_x/C and MnO_2 electrodes.

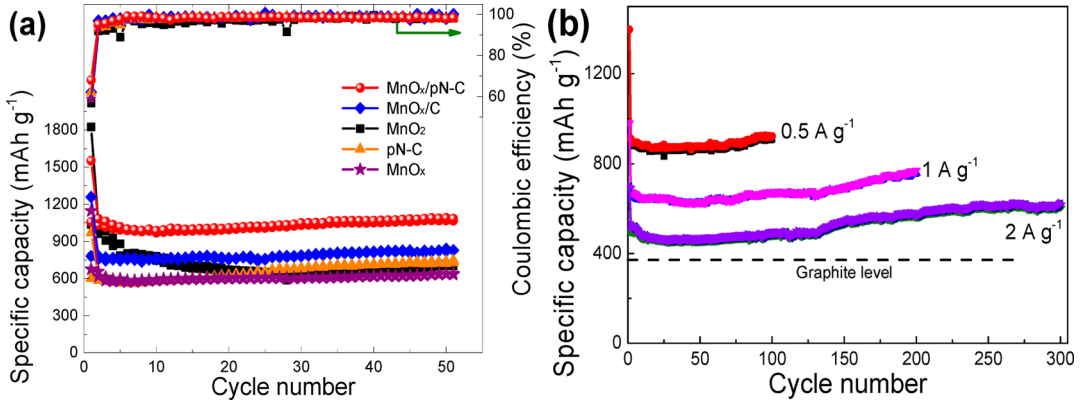

Figure 7. (a) Cycling comparison of MnO_x/pN-C, MnO_x/C, and MnO_2 electrodes at 100 mA g^{-1}. (b) Cycling performance of MnO_x/pN-C electrode at 0.5, 1, and 2 A g^{-1}.

discharge voltage profiles of MnO_x/pN-C, MnO_x/C, and MnO_2 electrodes at a constant current density of 100 mA g^{-1}. In the first cycle of the MnO_x/pN-C electrode, the discharge curve is composed of a short voltage plateau at ~0.7 V, a long plateau at ~0.25 V and a sloping curve down to the cutoff voltage of 0.005 V, which corresponds to the SEI layer formation and the reduction of MnO_x by Li^+ insertion, respectively. The discharge voltage plateau shifts to 0.4−0.5 V from the second cycle. These results are in good agreement with the CV analysis. It can be observed that the electrode delivers high lithium storage capacity of 1553 mAh g^{-1} and high reversible capacity of 1057 mAh g^{-1}. A capacity comparison for MnO_x/C and MnO_2 electrodes is observed to be 1159/782 and 1823/1037 mAh g^{-1}, respectively. The larger reversible capacity of the MnO_x/pN-C electrode suggests that the active materials provide more accessible sites for Li^+ insertion/extraction. The initial Coulombic efficiency of 68.1% is common and comparable to most carbon/metal oxide anodes (for details,

DOI: 10.1021/acsami.5b01388
ACS Appl. Mater. Interfaces 2015, 7, 9185−9194

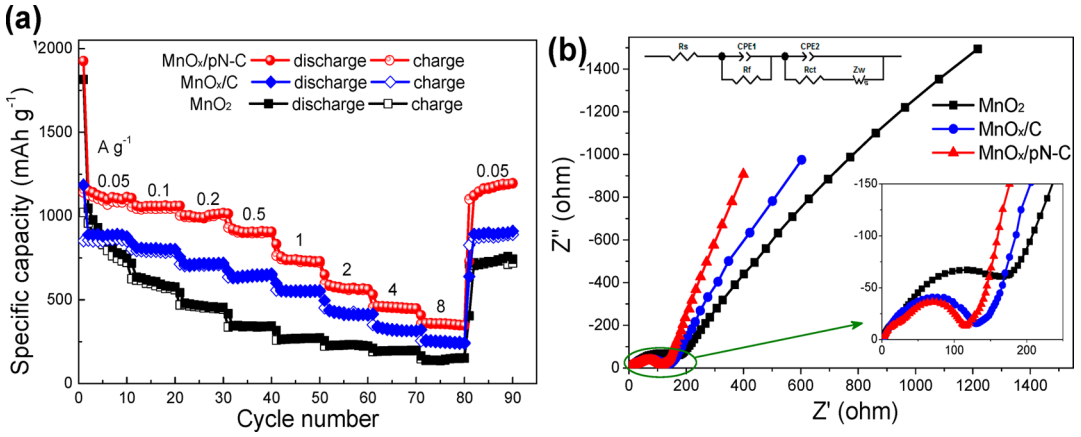

Figure 8. (a) Rate performance and (b) Nyquist plots of the MnO_x/pN-C, MnO_x/C, and MnO_2 electrodes; (inset) magnified view of Nyquist plot area indicated by the green circle.

see Table S1, Supporting Information) but still much higher than that of pure MnO_2 electrode (56.9%). The efficiency increases dramatically to 96% in the second cycle and remains over 98% thereafter. In addition, the irreversible capacity loss in the first cycle is caused by the inevitable formation of SEI film, the decomposition of electrolyte and/or some side reactions of pN-C with Li^+.[28,33] It is worth noting that there is a significant difference in the second and onward discharge curves between the MnO_x/pN-C electrode and the MnO_x/C and MnO_2 electrodes. As indicated by the shadow area shown in Figure 6(d), the discharge capacity of the MnO_x/pN-C electrode reaches 255 mAh g^{-1} in the potential range of 0.55−2.5 V, which is much larger than those of MnO_2 and MnO_x/C electrodes. Given that the active MnO_x component mainly contributes capacity in the potential below 0.55 V, the additional capacity is believed to be mostly from the pN-C component. The discharge profiles are also consistent with those of PPy-derived pN-C nanofibers.[28] This phenomenon indicates that the pN-C plays a remarkable electro-active role in the lithium storage process. In fact, pN-C possesses two factors that are responsible for the enhanced lithium storage capacity: (1) the high-level nitrogen doping creates a large quantity of electro-active sites, such as the pyridine-like defects with low energy barrier for Li^+ penetration and high surface affinity for Li^+ adsorption;[32] and (2) the highly porous structure provides numerous nanopore reservoirs for Li^+ storage and sufficient electrode/electrolyte interfaces for charge transference.

The cycling stability of the electrodes at a current density of 100 mA g^{-1} is displayed in Figure 7a. It is observed that the MnO_x/pN-C and MnO_x/C nanocomposite electrodes exhibit far superior capacity retention to that of bare MnO_2 electrode, suggestive of the effectiveness of surface carbon coating to promote cycling stability. In addition, the reversible capacity of the MnO_x/pN-C nanocomposite is much higher than those of bare MnO_x and pN-C, indicating a strong synergism between the MnO_x cores and the pN-C shells. The higher capacity with good cycling retention of the MnO_x/pN-C electrode can be rationalized by the wrapped pN-C coating, which is supposed to serve three functions: (1) enhance the electrochemical utilization of the nanocomposite by improving the electron-transfer kinetics and accommodating the large volume change of the underneath MnO_x during cycling, (2) facilitate the formation of a stable SEI layer by modifying the surface chemistry of MnO_x, and (3) offer additional electro-active sites for Li^+ storage. Moreover, the pure MnO_2 and MnO_x nanotubes, which are totally different from the MnO_x nanorods and nanoparticles,[46,47] show good cycling behavior after the initial degradation, presumably suggesting the nanotubular structure can, to some extent, offer adequate void space for accommodating the volume change of MnO_x. Interestingly, all electrodes show slightly increasing reversible capacities with further extended cycling, reaching 1068, 829, 704, 730, and 634 mAh g^{-1} in the 50th cycle for the MnO_x/pN-C, MnO_x/C, MnO_2, pN-C, and MnO_x electrodes, respectively. This phenomenon, as reported in the literature,[6,18,20,33,34,45] is considered to be related to the formation of a polymeric gel-like film resulting from kinetically activated electrolyte degradation and the increasing reaction activity of MnO_x during conversion process. The outstanding cycling stability of the MnO_x/pN-C electrode is further validated by the cycling tests at different current densities of 0.5, 1, and 2 A g^{-1}, as shown in Figure 7b. Encouragingly, even at a high current density of 2 A g^{-1}, a capacity of 606 mAh g^{-1} is retained after 300 discharge/charge cycles, which is still much higher than the theoretical capacity of graphite (372 mAh g^{-1}). Table S1 (Supporting Information) summarizes the recent lithium storage performance of MnO_x/C composites. The superior capacity and cycling performance of MnO_x/pN-C nanocomposite is much better than those of the most reported MnO_x/C anodes (Table S1, Supporting Information), particularly more advantageous when comparing with those using conventional carbon coating, such as MnO/C nanotubes/nanorods/nanoparticles/nanoplates[12−18,39] and Mn_3O_4/C nanorods,[7] indicating the unique pN-C coating is effective to promote the lithium storage properties.

In addition to the superior capacity and cyclability, the MnO_x/pN-C nanocomposite electrode shows remarkable rate capability. As shown in Figure 8a, the half cell was recorded for every 10 cycles at each progressively increased current density from 0.05 to 8 A g^{-1}. The nanocomposite electrode exhibits stable capacity at different current densities, even when suffering from sudden change of the current delivery. The average reversible capacities are 1086, 1045, 985, 913, 725, 566, 457, and 361 mAh g^{-1} at current densities of 0.05, 0.1, 0.2, 0.5, 1, 2, 4, and 8 A g^{-1}, respectively. Upon returning to 0.05 A g^{-1}, the capacity is recovered to ~1200 mAh g^{-1}, even higher than the value of the initial cycle. The impressive rate performance is much better than that of the control electrodes; for example, the MnO_2 electrode preserves only 17% (i.e., 140 mAh g^{-1}) of the initial average capacity at the high current density of 8 A

DOI: 10.1021/acsami.5b01388
ACS Appl. Mater. Interfaces 2015, 7, 9185−9194

g^{-1}. These results highlight the capability of the MnO_x/pN-C nanocomposite to meet the requirements of both long cycle life and high power delivery.

A better understanding of the rate capability of the nanocomposite electrode is obtained from EIS analysis. Figure 8b shows the resulting Nyquist plots of the MnO_x/pN-C and MnO_2 electrodes. The Nyquist profile of both electrodes shares the common feature of a depressed arc in the high-to-medium frequency region and a sloped line in the low-frequency region. The x intercept on the Z′ axis at the very high frequency represents the bulk solution resistance (R_s). The compressed arc can be generally decomposed into two arcs, the diameters of which are denoted as the SEI film resistance (R_f) at the high-frequency region and the charge transfer resistance (R_{ct}) at the medium-frequency region, respectively. The sloped line represents the Warburg impedance (Z_w) related to the lithium ions diffusion into the porous electrode. A simple equivalent circuit model (Figure 8b, inset) is built to fit the fundamental parameter values of the elements.[43] The fitting results are summarized in Table 1. The major difference is the R_{ct} in the nanocomposite electrode, which is only half of that in the MnO_2 electrode. The decreased R_{ct} reveals that the uniform pN-C coating provides improved electronic/ionic conductivity for fast charge transfer reactions. In addition, the sloped line of the nanocomposite electrode is steeper than that of the control one, which is indicative of a lower diffusion resistance for rapid Li^+ transport due to the highly porous structure. These results demonstrate favorable reaction kinetics in the nanocomposite electrode, thereby resulting in excellent rate capability. Furthermore, we have compared the EIS spectra of the nanocomposite electrode after different cycles to gain an insight into the capacity improvement (Figure S3, Supporting Information). There is a significant decrease of R_{ct} upon cycling. The decreased R_{ct} permits better contact between the active material and electrolyte, creates large electrode/electrolyte interface area for reaction sites, and reduces the internal resistance to improve the reaction kinetics.[19,44]

Table 1. Kinetic Parameters of MnO_x/pN-C and MnO_2 Electrodes

electrode	R_s (Ω)	R_f (Ω)	R_{ct} (Ω)	CPE1 (μF)	CPE2 (μF)
MnO_x/pN-C	3.62	25.87	91.12	8.26	60.53
MnO_x/C	3.68	27.16	104.29	7.42	37.36
MnO_2	3.75	29.35	197.58	3.69	25.4

Combining the high reversible capacity, excellent rate capability and long-term cycling stability, it is believed that the MnO_x/pN-C nanocomposite can serve as a good candidate of anode materials for high-performance LIBs. The outstanding electrochemical performance can be well-rationalized by the multifunctional components and their unique 1D nanoconfiguration. Figure 1b presents such a schematic illustrating the advantages, which include the following aspects. First, the high capacity can stem from the highly electro-active components, that is, (1) the pN-C coating with high-level N-doping provides a large quantity of active sites (e.g., nanopores and N-induced defects) for lithium storage, which is totally different from conventional carbon coatings; and (2) MnO_x makes considerable contribution to the overall capacity. Second, the high-rate performance is ascribed to the improved reaction kinetics: (1) the porous and nanotubular structure creates sufficient ion diffusion channels for fast Li^+ accessibility; (2) the 1D nanostructure shortens the solid transport pathways of Li^+ and electron for high-speed charge-transfer reactions; and (3) the N-enriched carbon coating with an intimate connection to the underneath MnO_x builds up electron transfer highways throughout the electrode. All these efforts promote maximum electrochemical harvest from the high-capacity components even under a high current density. Third, the long cycle life benefits from the core−shell configuration and hollow interior, specifically, (1) the uniform carbon coating not only acts as a "buffering zone" to cushion the large volume change of MnO_x during the lithiation/delithiation processes but also prevents the agglomeration and pulverization of nanostructures; and (2) the nanotubular structure affords free "void space" to digest partial volume variation.

4. CONCLUSIONS

In summary, we have successfully demonstrated a facile in situ chemically reactive template method to fabricate core−shell MnO_x/pN-C nanotubes. Owing to the high-level N-doping and porous structure, the uniform pN-C coating plays multiple roles in the nanocomposite, such as an electro-active component to improve the overall capacity, an elastic barrier to alleviate the stress of volume excursions and maintain the structural integrity, an electrically conducting network to boost the electron transfer, and a porous matrix to channel Li^+ accessing to the active sites. In combination with the unique nanosized and hollow structure, the MnO_x/pN-C nanocomposite anodes show remarkable lithium storage performance including high specific capacity, outstanding cyclability and excellent rate capability, which are highly desirable for advanced LIBs. The present design strategy also provides an effective and scalable way to develop other electrode materials with different nanostructures for energy storage/conversion systems.

■ ASSOCIATED CONTENT

Supporting Information

Table summarizing the cell performance of MnO_x-based anodes; TGA curves of MnO_x/pN-C, galvanostatic charge/discharge curves of MnO_x/C and MnO_2; and EIS spectra of MnO_x/pN-C after different cycles. This material is available free of charge via the Internet at http://pubs.acs.org.

■ AUTHOR INFORMATION

Corresponding Author

*Fax/Tel.: +86 29 88460361. E-mail: wangjiangan@nwpu.edu.cn.

Notes

The authors declare no competing financial interest.

■ ACKNOWLEDGMENTS

The authors acknowledge financial support from the National Natural Science Foundation of China (51402236 and 51232005), the Fundamental Research Funds for the Central Universities (3102014JCQ01020), the Research Fund of the State Key Laboratory of Solidification Processing (NWPU) (83-TZ-2013), and the Program of Introducing Talents of Discipline to Universities (B08040). We also appreciate the financial support from the Guangdong Province Innovation R&D Team Plan.

DOI: 10.1021/acsami.5b01388
ACS Appl. Mater. Interfaces 2015, 7, 9185−9194

REFERENCES

(1) Yang, Z.; Zhang, J.; Kintner-Meyer, M. C. W.; Lu, X.; Choi, D.; Lemmon, J. P.; Liu, J. Electrochemical Energy Storage for Green Grid. *Chem. Rev.* **2011**, *111*, 3577−3613.

(2) Etacheri, V.; Marom, R.; Elazari, R.; Salitra, G. Aurbach, Challenges in the Development of Advanced Li-Ion Batteries: A Review. D. *Energy Environ. Sci.* **2011**, *4*, 3243−3262.

(3) Kim, T.-H.; Park, J.-S.; Chang, S. K.; Choi, S.; Ryu, J. H.; Song, H.-K. The Current Move of Lithium Ion Batteries Towards the Next Phase. *Adv. Energy Mater.* **2012**, *2*, 860−872.

(4) Ji, L.; Lin, Z.; Alcoutlabi, M.; Zhang, X. Recent Developments in Nanostructured Anode Materials for Rechargeable Lithium-Ion Batteries. *Energy Environ. Sci.* **2011**, *4*, 2682−2699.

(5) Reddy, M. V.; Rao, G. V. S.; Chowdari, B. V. R. Metal Oxides and Oxysalts as Anode Materials for Li Ion Batteries. *Chem. Rev.* **2013**, *113*, 5364−5457.

(6) Liu, B.; Hu, X.; Xu, H.; Luo, W.; Sun, Y.; Huang, Y. Encapsulation of MnO Nanocrystals in Electrospun Carbon Nanofibers as High-Performance Anode Materials for Lithium-Ion Batteries. *Sci. Rep.* **2013**, *4*, 4299.

(7) Wang, C.; Yin, L.; Xiang, D.; Qi, Y. Uniform Carbon Layer Coated Mn_3O_4 Nanorod Anodes with Improved Reversible Capacity and Cyclic Stability for Lithium Ion Batteries. *ACS Appl. Mater. Interfaces* **2012**, *4*, 1636−1642.

(8) Mai, Y.; Zhang, D.; Qiao, Y.; Gu, C.; Wang, X.; Tu, J. MnO/Reduced Graphene Oxide Sheet Hybrid as an Anode for Li-ion Batteries with Enhanced Lithium Storage Performance. *J. Power Sources* **2012**, *216*, 201−207.

(9) Li, L.; Nan, C.; Lu, J.; Peng, Q.; Li, Y. α-MnO_2 Nanotubes: High Surface Area and Enhanced Lithium Battery Properties. *Chem. Commun.* **2012**, *48*, 6945−6947.

(10) Wang, J.; Du, N.; Wu, H.; Zhang, H.; Yu, J.; Yang, D. Order-Aligned Mn_3O_4 Nanostructures as Super High-Rate Electrodes for Rechargeable Lithium-Ion Batteries. *J. Power Sources* **2012**, *222*, 32−37.

(11) Reddy, A. L. M.; Shaijumon, M. M.; Gowda, S. R.; Ajayan, P. M. Coaxial MnO_2/Carbon Nanotube Array Electrodes for High-Performance Lithium Batteries. *Nano Lett.* **2009**, *9*, 1002−1006.

(12) Li, X.; Xiong, S.; Li, J.; Liang, X.; Wang, J.; Bai, J.; Qian, Y. MnO@Carbon Core−Shell Nanowires as Stable High-Performance Anodes for Lithium-Ion Batteries. *Chem.—Eur. J.* **2013**, *19*, 11310−11319.

(13) Sun, B.; Chen, Z.; Kim, H.-S.; Ahn, H.; Wang, G. MnO/C Core−Shell Nanorods as High Capacity Anode Materials for Lithium-Ion Batteries. *J. Power Sources* **2011**, *196*, 3346−3349.

(14) Su, L.; Zhong, Y.; Wei, J.; Zhou, Z. Preparation and Electrochemical Li Storage Performance of MnO@C Nanorods Consisting of Ultra Small MnO Nanocrystals. *RSC Adv.* **2013**, *3*, 9035−9041.

(15) Xu, G.-L.; Xu, Y.-F.; Sun, H.; Fu, F.; Zheng, X.-M.; Huang, L.; Li, J.-T.; Yang, S.-H.; Sun, S.-G. Facile Synthesis of Porous MnO/C Nanotubes as a High Capacity Anode Material for Lithium Ion Batteries. *Chem. Commun.* **2012**, *48*, 8502−8504.

(16) Ding, Y.; Wu, C.; Yu, H.; Xie, J.; Cao, G.; Zhu, T.; Zhao, X.; Zeng, Y. Coaxial MnO/C Nanotubes as Anodes for Lithium-Ion Batteries. *Electrochim. Acta* **2011**, *56*, 5844−5848.

(17) Zhang, X.; Xing, Z.; Wang, L.; Zhu, Y.; Li, Q.; Liang, J.; Yu, Y.; Huang, T.; Tang, K.; Qian, Y. Synthesis of MnO@C Core−Shell Nanoplates with Controllable Shell Thickness and their Electrochemical Performance for Lithium-Ion Batteries. *J. Mater. Chem.* **2012**, *22*, 17864−17869.

(18) Gu, X.; Yue, J.; Chen, L.; Liu, S.; Xu, H.; Yang, J.; Qian, Y.; Zhao, X. Coaxial MnO/N-Doped Carbon Nanorods for Advanced Lithium-Ion Battery Anodes. *J. Mater. Chem. A* **2015**, *3*, 1037−1041.

(19) Zhang, K.; Han, P.; Gu, L.; Zhang, L.; Liu, Z.; Kong, Q.; Zhang, C.; Dong, S.; Zhang, Z.; Yao, J. Synthesis of Nitrogen-Doped MnO/Graphene Nanosheets Hybrid Material for Lithium Ion Batteries. *ACS Appl. Mater. Interfaces* **2012**, *4*, 658−664.

(20) Sun, Y.; Hu, X.; Luo, W.; Xia, F.; Huang, Y. Reconstruction of Conformal Nanoscale MnO on Graphene as a High-Capacity and Long-Life Anode Material for Lithium Ion Batteries. *Adv. Funct. Mater.* **2013**, *23*, 2436−2444.

(21) Yu, A.; Par, H. W.; Davies, A.; Higgins, D. C.; Chen, Z.; Xiao, X. Free-Standing Layer-By-Layer Hybrid Thin Film of Graphene-MnO_2 Nanotube as Anode for Lithium Ion Batteries. *J. Phys. Chem. Lett.* **2011**, *2*, 1855−1860.

(22) Hsieh, C.-T.; Lin, C.-Y.; Lin, J.-Y. Reversibility of Li Intercalation and De-intercalation in MnO-Attached Graphene Anodes for Li-Ion Batteries. *Electrochim. Acta* **2011**, *56*, 8861−8867.

(23) Xia, H.; Lai, M.; Lu, L. Nanoflaky MnO_2/Carbon Nanotube Nanocomposites as Anode Materials for Lithium-Ion Batteries. *J. Mater. Chem.* **2010**, *20*, 6896−6902.

(24) Qin, J.; Zhang, Q.; Cao, Z.; Li, X.; Hu, C.; Wei, B. MnO_x/SWCNT Macro-Films as Flexible Binder-Free Anodes for High-Performance Li-Ion Batteries. *Nano Energy* **2013**, *2*, 733−741.

(25) Luo, S.; Wu, H.; Wu, Y.; Jiang, K.; Wang, J.; Fan, S. Mn_3O_4 Nanoparticles Anchored on Continuous Carbon Nanotube Network as Superior Anodes for Lithium Ion Batteries. *J. Power Sources* **2014**, *249*, 463−469.

(26) Ji, L.; Zhang, X. Manganese Oxide Nanoparticle-Loaded Porous Carbon Nanofibers as Anode Materials for High-Performance Lithium-Ion Batteries. *Electrochem. Commun.* **2009**, *11*, 795−798.

(27) Ji, L.; Medford, A. J.; Zhang, X. Porous Carbon Nanofibers Loaded with Manganese Oxide Particles: Formation Mechanism and Electrochemical Performance as Energy-Storage Materials. *J. Mater. Chem.* **2009**, *19*, 5593−5601.

(28) Qie, L.; Chen, W. M.; Wang, Z. H.; Shao, Q. G.; Li, X.; Yuan, L. X.; Hu, X. L.; Zhang, W. X.; Huang, Y. H. Nitrogen-Doped Porous Carbon Nanofiber Webs as Anodes for Lithium Ion Batteries with a Superhigh Capacity and Rate Capability. *Adv. Mater.* **2012**, *24*, 2047−2050.

(29) Nan, D.; Huang, Z.-H.; Lv, R.; Yang, L.; Wang, J.-G.; Shen, W.; Lin, Y.; Yu, X.; Ye, L.; Sun, H.; Kang, F. Nitrogen-enriched Electrospun Porous Carbon Nanofiber Networks as High-Performance Free-Standing Electrode Materials. *J. Mater. Chem. A* **2014**, *2*, 19678−19684.

(30) Reddy, A. L. M.; Srivastava, A.; Gowda, S. R.; Gullapalli, H.; Dubey, M.; Ajayan, P. M. Synthesis of Nitrogen-Doped Graphene Films for Lithium Battery Application. *ACS Nano* **2010**, *4*, 6337−6342.

(31) Li, X.; Geng, D.; Zhang, Y.; Meng, X.; Li, R.; Sun, X. Superior Cycle Stability of Nitrogen-Doped Graphene Nanosheets as Anodes for Lithium Ion Batteries. *Electrochem. Commun.* **2011**, *13*, 822−825.

(32) Shin, W. H.; Jeong, H. M.; Kim, B. G.; Kang, J. K.; Choi, J. W. Nitrogen-Doped Multiwall Carbon Nanotubes for Lithium Storage with Extremely High Capacity. *Nano Lett.* **2012**, *12*, 2283−2288.

(33) Chen, W.-M.; Qie, L.; Shen, Y.; Sun, Y.-M.; Yuan, L.-X.; Hu, X.-L.; Zhang, W.-X.; Huang, Y.-H. Superior Lithium Storage Performance in Nanoscaled MnO Promoted by N-Doped Carbon Webs. *Nano Energy* **2013**, *2*, 412−418.

(34) Xiao, Y.; Wang, X.; Wang, W.; Zhao, D.; Cao, M. Engineering Hybrid between MnO and N-Doped Carbon to Achieve Exceptionally High Capacity for Lithium-Ion Battery Anode. *ACS Appl. Mater. Interfaces* **2014**, *6*, 2051−2058.

(35) Wang, J.-G.; Yang, Y.; Huang, Z.-H.; Kang, F. Shape-Controlled Synthesis of Hierarchical Hollow Urchin-Shape α-MnO_2 Nanostructures and their Electrochemical Properties. *Mater. Chem. Phys.* **2013**, *140*, 643−650.

(36) Wang, J.-G.; Wei, B.; Kang, F. Facile Synthesis of Hierarchical Conducting Polypyrrole Nanostructures via a Reactive Template of MnO_2 and their Application in Supercapacitors. *RSC Adv.* **2014**, *4*, 199−202.

(37) Li, J.; Cui, L.; Zhang, X. Preparation and Electrochemistry of One-Dimensional Nanostructured MnO_2/PPy Composite for Electrochemical Capacitor. *Appl. Surf. Sci.* **2010**, *256*, 4339−4343.

(38) Gao, J.; Lowe, M. A.; Abruña, H. D. Spongelike Nanosized Mn_3O_4 as a High-Capacity Anode Material for Rechargeable Lithium Batteries. *Chem. Mater.* **2011**, *23*, 3223−3227.

DOI: 10.1021/acsami.5b01388
ACS Appl. Mater. Interfaces 2015, 7, 9185−9194

(39) Li, S.-R.; Sun, Y.; Ge, S.-Y.; Qiao, Y.; Chen, Y.-M.; Lieberwirth, I.; Yu, Y.; Chen, C.-H. A Facile Route to Synthesize Nano-MnO/C Composites and their Application in Lithium Ion Batteries. *Chem. Eng. J.* **2012**, *192*, 226−231.
(40) Wang, J.-G.; Yang, Y.; Huang, Z.-H.; Kang, F. Effect of Temperature on the Pseudo-Capacitive Behavior of Freestanding MnO_2@Carbon Nanofibers Composites Electrodes in Mild Electrolyte. *J. Power Sources* **2013**, *224*, 86−92.
(41) Toupin, M.; Brousse, T.; Bélanger, D. Charge Storage Mechanism of MnO_2 Electrode Used in Aqueous Electrochemical Capacitor. *Chem. Mater.* **2004**, *16*, 3184−3190.
(42) Jeong, H. M.; Lee, J. W.; Shin, W. H.; Choi, Y. J.; Shin, H. J.; Kang, J. K.; Choi, J. W. Nitrogen-Doped Graphene for High-Performance Ultracapacitors and the Importance of Nitrogen-Doped Sites at Basal Planes. *Nano Lett.* **2011**, *11*, 2472−2477.
(43) Qie, L.; Chen, W.; Xu, H.; Xiong, X.; Jiang, Y.; Zou, F.; Hu, X.; Xin, Y.; Zhang, Z.; Huang, Y. Synthesis of Functionalized 3D Hierarchical Porous Carbon for High-Performance Supercapacitors. *Energy Environ. Sci.* **2013**, *6*, 2497−2504.
(44) Xia, Y.; Xiao, Z.; Dou, X.; Huang, H.; Lu, X.; Yan, R.; Gan, Y.; Zhu, W.; Tu, J.; Zhang, W.; Tao, X. Green and Facile Fabrication of Hollow Porous MnO-C Microspheres from Microalgaes for Lithium-Ion Batteries. *ACS Nano* **2013**, *7*, 7083−7092.
(45) Li, X.; Zhu, Y.; Zhang, X.; Liang, J.; Qian, Y. MnO@1-D Carbon Composites from the Precursor $C_4H_4MnO_6$ and their High-Performance in Lithium Batteries. *RSC Adv.* **2013**, *3*, 10001−10006.
(46) Cheng, F.; Zhao, J.; Song, W.; Li, C.; Ma, H.; Chen, J.; Shen, P. Low-Temperature Synthesis of α-MnO_2 Hollow Urchins and their Application in Rechargeable Li^+ Batteries. *Inorg. Chem.* **2006**, *45*, 2038−2044.
(47) Zhao, J.; Tao, Z.; Liang, J.; Chen, J. Facile Synthesis of Nanoporous γ-MnO_2 Structures and Their Application in Rechargeable Li-Ion Batteries. *Cryst. Growth Des.* **2008**, *8*, 2799−2805.

DOI: 10.1021/acsami.5b01388
ACS Appl. Mater. Interfaces 2015, 7, 9185−9194